

2018-10-16

Threshold for discretely self-similar satellite drop formation from a retracting liquid cone

C Frederik Brasz, Alexis Berny, James C Bird. 2018. "Threshold for discretely self-similar satellite drop formation from a retracting liquid cone." *Physical Review Fluids*, Volume 3, Issue 10, 13 pages. <https://doi.org/10.1103/PhysRevFluids.3.104002>

<https://hdl.handle.net/2144/41142>

"Downloaded from OpenBU. Boston University's institutional repository."

Threshold for discretely self-similar satellite drop formation from a retracting liquid cone

C. Frederik Brasz*, Alexis Berny, and James C. Bird†

Department of Mechanical Engineering, Boston University, Boston, MA 02215, USA

Received 19 April 2018; published 16 October 2018

Abstract

Predicting the size of droplets that pinch off from a liquid jet is important to applications ranging from bubble-initiated atmospheric aerosols to inkjet printing. These predictions are complicated by smaller satellite drops that form when a thin liquid thread develops and breaks up faster than its ends fully retract. Typically this process is modeled by perturbing a cylindrical liquid thread with an amplitude that is small relative to the cylinder diameter. Yet early on in the pinch-off process, the ends of the liquid thread are conical and lack a characteristic length scale from which to normalize a finite perturbation. Here we numerically simulate the retraction of nearly-inviscid conical filaments and introduce self-similar perturbations to drive the system into a discretely self-similar retraction that can enable breakup without biasing a particular length scale. We find that for most cone angles, the perturbation amplitude must exceed a threshold for satellite drops to form. We show that this critical perturbation amplitude depends on the cone angle and can be accurately predicted by an argument based on the static stability of the initial perturbed cone.

1 Introduction

The breakup of fluid filaments into drops occurs in a wide variety of natural and controlled contexts, from inkjet printing [1, 2, 3] and fuel injection [4] to irrigation and sea spray aerosol production [5]. For the case of sea spray aerosol production, breaking waves entrain bubbles that burst at the surface to eject droplets; the smaller drops can be carried to the atmosphere as aerosol particles, where they scatter radiation and act as cloud condensation nuclei [5, 6]. A significant fraction of these aerosol particles is attributed to jet drops, which are produced by the breakup of a jet that shoots upward from the bursting bubble as the bubble cavity collapses [7, 8]. Of particular interest is the production of submicron aerosols from jet drops [9]; yet efforts to predict size have been limited to top jet drops [10, 11], with the tacit assumption that subsequent drops are of the same order of magnitude. On occasion, droplets smaller than expected have been observed, prompting speculation that these are smaller satellite drops that form between larger primary drops during the pinch-off process [12, 13, 5]. Indeed, size distributions of jet drops from sub-100 μm bubbles [9] reveal drops up to an order of magnitude smaller than expected from the minimum size for top jet drops [11], which might be explained by the presence of satellite drops. However, despite extensive progress in the understanding of liquid jets and breakup [14, 15], the conditions required for low viscosity filaments to form satellite drops early on in the pinch-off process remain unclear.

*cfbrasz@gmail.com

†jbird@bu.edu

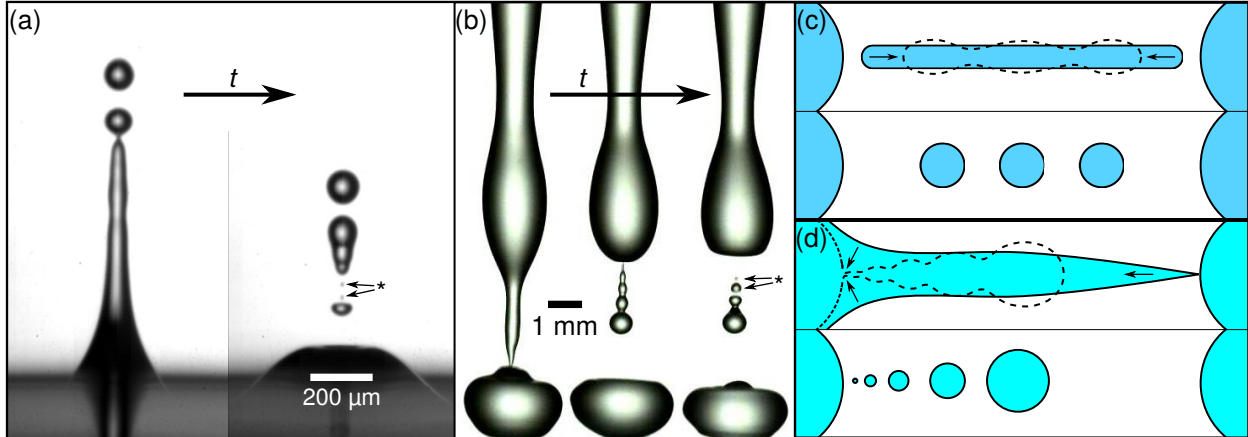


Figure 1: Examples and schematics of satellite and subsatellite droplet formation at various times t . (a) Two snapshots of the jet and drops ejected by a bubble bursting at an air-water interface. After the jet pinches off at the base, the remaining filament pinches off into smaller satellite drops, highlighted by asterisks (*). (b) Sequence of images of a stream of water released from a syringe, with a filament breaking up into satellite and subsatellite drops after pinching off from the main drop. (c) Schematic of a cylindrical ligament of liquid, before and after breaking up into droplets. (d) Schematic of pinch-off of a ligament leading to a sequence of satellite drops. The first pinch-off event (top right) is stable and does not create satellite drops. However, it initiates capillary waves, which perturb the remaining conical filament at pinch-off (top left). For a significant enough perturbation, the remaining filament could break up into satellite and subsatellite drops.

Figure 1(a) shows images of drop formation resulting from a bubble bursting at a water surface that we obtain with a high-speed camera. The collapsing bubble cavity inverts to shoot a jet upward, ejecting multiple jet drops. The jet eventually pinches off near the base, and two satellite drops much smaller than the main jet drops are visible. We observe similar behavior at a slightly larger scale when a column of water released from a syringe breaks up via the Plateau-Rayleigh instability [Fig. 1(b)]. A thin filament detaches from the drop at the bottom, initiating capillary waves that perturb the filament as it retracts due to surface tension. The other end of the filament then pinches off with a perturbed conical shape, and subsatellite drops form as it retracts (see this sequence and similar pinching events in movie 1 in the Supplemental Material [16]).

Previous studies have investigated satellite drop formation by examining the dynamics of retracting cylindrical liquid filaments. By varying aspect ratios and fluid properties, the filament will either retract into a single drop or break up into multiple drops as a result of the Plateau-Rayleigh instability or end-pinching [17, 18, 19, 20]. This breakup process is illustrated schematically in Fig. 1(c). Yet Fig. 1(b) suggests that in some cases, a conical filament may be a more relevant shape to study for the production of the smallest satellite drops early on in the pinch-off process. As a column of inviscid liquid approaches pinch-off, the local interface for both the thin filament and the drop develop conical shapes, with angles of 18.1° and 112.8° respectively, measured from the axis of symmetry [21]. After breakup, the conical filament retracts, and both pre- and post-pinch-off solutions are self-similar, with profiles collapsing when lengths are rescaled by $t^{-2/3}$, where t is the time before or after pinch-off [22, 23]. This self-similar solution exhibits capillary waves near the tip, but numerical [24] and experimental [25] evidence suggests it to be stable in the conical regime with minimal perturbations. However, if the retracting cone is noticeably perturbed—for example by capillary waves from an earlier pinch-off event converging to a later pinch-off event [25, 26]—the cone can break up into subsatellite drops [27] [Fig. 1(b), (d)]. Thus, a natural question is how large a perturbation is necessary for a liquid cone to break up while retracting.

To address this question, this paper aims to incorporate concepts from the self-similar inviscid cone

retraction literature with the cylindrical filament breakup literature. A nonzero initial perturbation amplitude is required (and unavoidable, practically speaking) for a cylindrical filament to break up via the Plateau-Rayleigh instability. An initial perturbation amplitude of 1% of the cylinder radius worked well [19] in making both linear theory and numerical simulations (using the slender jet approximation [28, 29]) match corresponding experimental results [18]. A challenge with extending this framework to conical filaments is the lack of a characteristic length scale to peg the initial perturbation amplitude. We therefore construct a self-similar perturbation to numerically investigate the perturbation amplitude required for the retracting cone to break up into multiple droplets. Because the cone angle at pinch-off can vary [30] [Fig. 1], we compute the critical amplitude as a function of the cone angle. Finally, we relate the threshold for breakup with a predictive model based on the static stability of the initial perturbation geometry.

2 Numerical setup

By working with a cone rather than a cylinder, there is no single radius and hence no characteristic length scale. Thus, adding a perturbation to a cone requires some finesse to avoid privileging a particular length scale. We therefore seek to define a perturbation independent of length scale as well. Starting with an unperturbed cone defined in cylindrical coordinates as $r(z) = z \tan \theta$, we add a sinusoidal perturbation with phase $\phi(z)$ and amplitude proportional to the local radius to obtain

$$r(z) = z \tan \theta (1 + \epsilon \sin \phi(z)). \quad (1)$$

The local wavelength of the perturbation can be obtained from the phase $\phi(z)$ as $\lambda(z) = 2\pi / (d\phi/dz)$. To make the perturbation self-similar, we require that the wavelength is also proportional to the (unperturbed) local radius by setting $\lambda(z) \equiv \lambda^* z \tan \theta$. This choice leads to the phase function taking the form

$$\phi(z) = \frac{2\pi}{\lambda^* \tan \theta} \log z + \phi_0, \quad (2)$$

where ϕ_0 is an arbitrary phase offset.

The initial geometry of the perturbed cone is then prescribed by Eqs. (1) and (2) with independent parameters θ , ϵ , and λ^* setting the cone angle, relative perturbation amplitude, and dimensionless wavelength respectively. For simulation purposes, we cut off the cone at some largest (unperturbed) radius R and truncate it below some minimum radius R_n set by the grid resolution. Figure 2 shows a schematic of the initial geometry. As desired, the perturbation appears self-similar over multiple iterations of magnification. Specifically, the profile remains the same when lengths are rescaled by the ratio r_l raised to some integer power, where $r_l = \exp(-\lambda^* \tan \theta)$. This ratio is effectively the log-space version of the perturbation wavelength, which is constant. Figure 2(b) and 2(c) illustrate the fractal structure that this initial perturbation exhibits. We note that we use symmetry about $z = Z \equiv R / \tan \theta$, which means we are simulating the retraction of a double cone. While this geometry differs from the experiment and schematic in Figs. 1(b) and (d), it is similar to the symmetry of cylindrical filament studies. Furthermore, the evolution at smaller scales occurs much faster than at the largest scale, so the effects of replacing this symmetry condition with a spherical cap are expected to be small. Finally, the cone is initialized at rest for simplicity. We note that the self-similar solution for an unperturbed retracting cone does change when the far-field velocity from the pre-pinching solution is included [22], but using the pre-pinching solution also restricts us to a single cone angle; starting from rest allows for greater generality with arbitrary angles.

To probe the stability of the perturbed cone, we simulate its evolution with the open-source fluid solver Gerris [31, 32, 33]. Gerris solves the incompressible Navier-Stokes equations with a fractional-step projection method, using an adaptive quad/octree spatial discretization and a multilevel Poisson solver. The interface between liquid and gas is captured by a volume of fluid (VOF) scheme, and its accurate surface tension model makes Gerris well-suited for capillary breakup problems [33, 20]. Additional details on the setup and validation of numerical simulations are provided in the Supplemental Material.

We focus on the effects of varying θ and ϵ , taking $\lambda^* = 2\pi$ as a representative relative wavelength because $2\pi R$ is the minimum wavelength required for a perturbation to a cylinder of radius R to be unstable. The

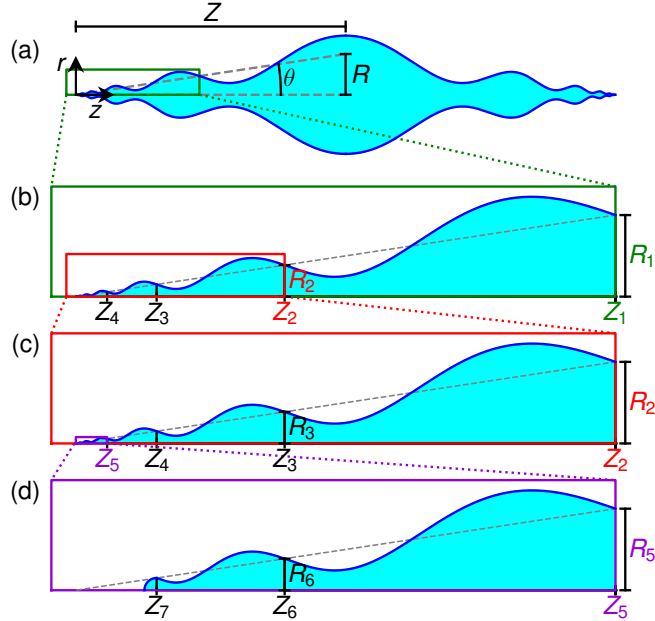


Figure 2: Schematic of the initial geometry for cone angle $\theta = 0.15$ rad (8.59°), perturbation amplitude $\epsilon = 0.5$, and relative wavelength $\lambda^* = 2\pi$. (a) To numerically simulate the cone evolution, a maximum radius R and half-length Z are defined. Zooming in along successively smaller regions [(b)–(d)] demonstrates the cyclic self-similarity of the profile. The self-similarity is truncated after the seventh wave by a spherical cap.

density ratio ρ_r and viscosity ratio μ_r of the outer fluid to the liquid cone are taken as the values for water in air, $\rho_r = 0.0012$ and $\mu_r = 0.018$. The Ohnesorge number $\text{Oh} \equiv \mu/\sqrt{\rho\gamma R}$, where μ , ρ , and γ are respectively the liquid viscosity, density, and surface tension, is set at 0.001, corresponding to maximum radius of $R = 1.4$ cm for water. For the case of Fig. 2, $r_l = 0.387$ and $R_7 = 22$ μm . These length scales are somewhat large relative to typical liquid filaments, but we emphasize that the aim of the paper is to investigate the fundamental dynamics of perturbed retracting cones, and smaller Ohnesorge numbers allow for improved clarity of the observed dynamics.

3 Discrete self-similarity

With a cone angle of $\theta = 0.15$ and no perturbation ($\epsilon = 0$), the retraction is depicted in unscaled form in Fig. 3(a). Scaling the profiles with similarity variables $\bar{r} \equiv r/(t^2\gamma/\rho)^{1/3}$ and $\bar{z} \equiv z/(t^2\gamma/\rho)^{1/3}$, we recover the inviscid self-similarity [22] in Fig. 3(b) as an intermediate asymptotic behavior between the limiting scales R_n and R [34, 24]. The small deviation from the inviscid self-similar solution [22] is due to the nonzero value of $\text{Oh} = 10^{-3}$ used; Figure 6 in Appendix B shows that the agreement improves with smaller values of Oh .

Adding a perturbation of amplitude $\epsilon = 0.5$, Fig. 3(c) depicts the time evolution of the retracting cone, with time increasing from top to bottom (see also movie 2 in [16]). We immediately see that for this angle, the perturbation amplitude $\epsilon = 0.5$ is indeed sufficient to cause the cone to break up into drops, starting with small drops at early times and larger drops at later times. The filament appears to cycle between two and three drops, as the smallest drop coalesces with the next smallest drop just prior to a new drop pinching off.

The cyclical nature of these profiles is emphasized by the choice of geometrically-scaled times plotted. If viscosity can be neglected, the characteristic time associated with a length scale R_n is given by the capillary time $\tau_n = \sqrt{\rho R_n^3/\gamma}$. One can therefore define a temporal scaling ratio for successive waves of the perturbation by $r_t \equiv \tau_{n+1}/\tau_n = r_l^{3/2}$. This ratio is used to pick the times plotted in Fig. 3(c). The earliest

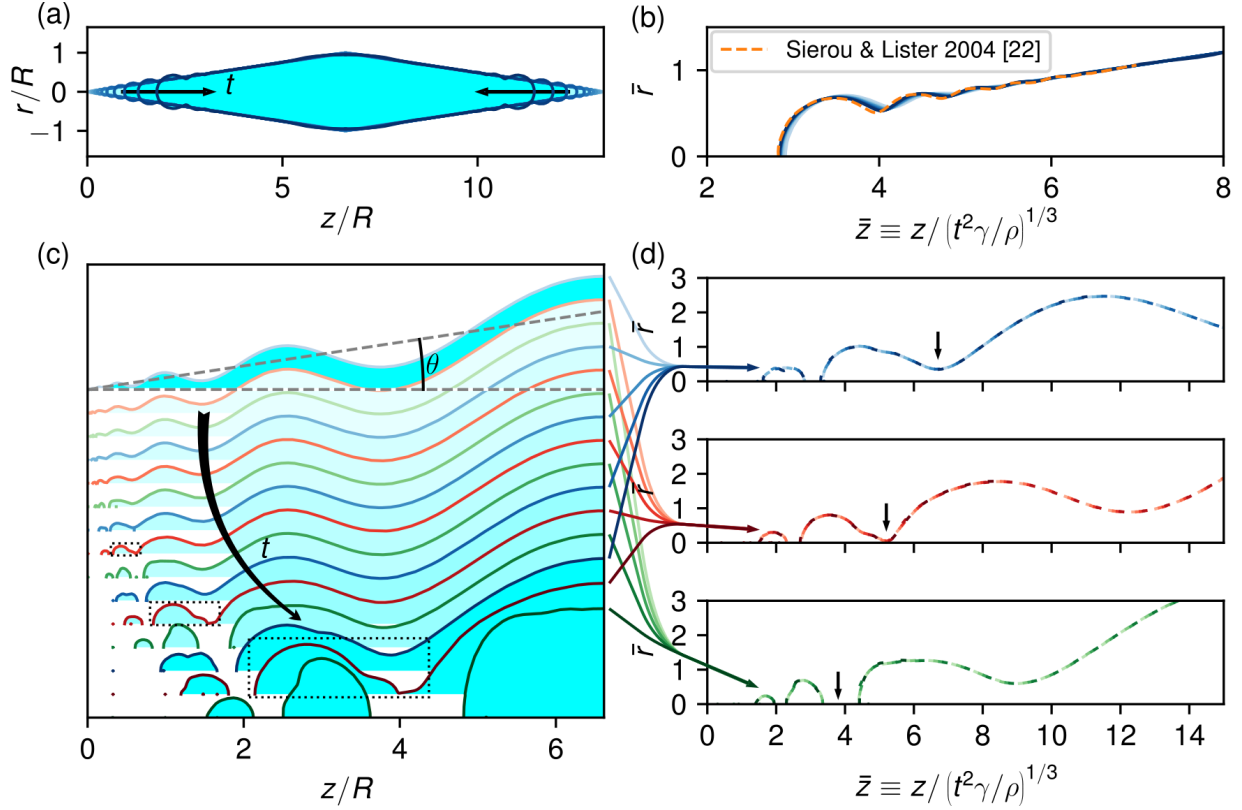


Figure 3: Profile snapshots for $\theta = 0.15$ with no perturbation ($\epsilon = 0$, top) and with $\epsilon = 0.5$ (bottom). Successive times are plotted both in the original coordinate system (left) and with the self-similar scaling (right). (a) With no perturbation, the tips grow as they retract. (b) The profiles collapse when scaled in the self-similar form $\bar{r} \equiv r/(t^2\gamma/\rho)^{1/3}$ and $\bar{z} \equiv z/(t^2\gamma/\rho)^{1/3}$, and they compare well with the inviscid self-similar solution of Ref. [22]. (c) For $\epsilon = 0.5$, profiles are offset from each other based on time, with t increasing from top to bottom. The times plotted are t_0/r_t^i for $i = 0-4$ for the blue curves, and $t_0/r_t^{i+1/3}$ and $t_0/r_t^{i+2/3}$ for the red and green curves, respectively. Dotted boxes highlight the red profiles with drops about to pinch off taking the same shape. (d) When plotted in self-similar form, the blue, red, and green curves all collapse, illustrating the discrete self-similarity of the retracting cone. The black arrows emphasize the repeated thinning and breakup of the neck near $\bar{z} = 5$.

time (lightest blue curve) corresponds to $t_0 = 0.00148\tau$, where $\tau \equiv \sqrt{\rho R^3/\gamma}$, and the times of subsequent blue curves are t_0/r_t^i for $i = 1-4$. The times of the red and green curves are respectively $t_0/r_t^{i+1/3}$ and $t_0/r_t^{i+2/3}$, showing different phases within the cycle. The dashed box around the largest detached drop in the last three green profiles highlights the similarity of the drop shape.

Collecting all of the blue, red, and green profiles together and applying the same self-similar scaling used for the unperturbed cone, we see in Fig. 3(d) that the profiles collapse well over these five cycles (see also movie 3 in [16]). Importantly, the profiles are only self-similar when the ratio of their times is an integer power of the temporal scaling ratio r_t . This cyclical self-similar scaling has been called a discrete self-similarity or discrete scale invariance [35] and observed in gravitational collapse [36], satellite drop [37] and neck formation in the breakup of viscous jets [38, 39], coalescence of metal spheres [40], beads-on-a-string formation in viscoelastic jets [41] and rupturing thin films [42]. For the case of rupturing thin films, the discrete self-similarity was shown to appear via a Hopf bifurcation from continuously self-similar solutions [42].

An important distinction to make between our discrete self-similarity and others reported in the literature is that the discrete self-similarity develops spontaneously in other cases, while we explicitly introduce an initial self-similar perturbation that drives the discrete self-similarity. It is thus not too surprising that we observe a discrete self-similarity, although we show below that for a small enough angle, the retracting cone does not enter a self-similar state at all. Note also that numerical simulations of viscous jet breakup required an external noise source to induce repeated neck formation [38]; the amplitude of the noise was only around 10^{-4} times the minimum neck thickness, however. In our case, we are particularly interested in the amplitude of the initial perturbation required for discretely self-similar breakup of the cone.

A convenient way to describe the discrete self-similarity of the profiles is by defining a logarithmic time $\bar{t} \equiv \log(t/t_0)$. In this logarithmic time, the scaled profiles display periodicity with period $T \equiv \log(1/r_t) = (3/2)\lambda^* \tan \theta$. The blue profiles in Figs. 3(c)–(d) all occur at $\bar{t} = 0 \pmod{T}$, while the red and green profiles respectively correspond to $\bar{t} = (1/3)T \pmod{T}$ and $\bar{t} = (2/3)T \pmod{T}$. The collapse of profiles suggests that our initial perturbation evolves into a discretely self-similar profile that can be described in parametric form with parameter s as $\bar{r}(s, \bar{t})$ and $\bar{z}(s, \bar{t})$, which are both periodic in \bar{t} with period T . We see that the initial perturbation effectively imposes an oscillating far-field boundary condition on the scaled problem, forcing the solution to oscillate at the same frequency in logarithmic time. Note that the number of periods over which the interface exhibits this discrete self-similarity is constrained by the number of waves defined by the initial perturbation.

Simulations with larger (smaller) Oh result in somewhat worse (better) collapse between profiles, and the variation in the local Ohnesorge number $\text{Oh}_n \equiv \mu/\sqrt{\rho\gamma R_n}$ with radius R_n also leads to differences between early and late cycles of a single simulation. As Oh_n increases, either by choosing a larger Oh or by focusing on an earlier cycle of the perturbation (with smaller length scale R_n), the pinch-off process is delayed and eventually suppressed, and capillary waves are dampened more. The delayed pinch-off in earlier cycles relative to later cycles is illustrated by the profiles in Fig. 7 in Appendix B. The rather small value of $\text{Oh} = 0.001$ was chosen to highlight the discrete self-similarity over many cycles while still preventing R from being unreasonably large for typical liquid properties.

4 Threshold for breakup

Having established in Fig. 3 that a large enough self-similar perturbation causes a retracting cone to break up into drops, we now seek the critical perturbation amplitude for breakup as a function of cone angle. Simulations are run for angles θ ranging from 1° to 20° , with 4 perturbation amplitudes ϵ for each angle. The results are summarized in Fig. 4(a); each red ‘x’ denotes a simulation in which the cone retracts without any drops pinching off, while cyan circles denote simulations in which pinch-off occurs. The radius of the circle corresponds to the volume-equivalent radius of the largest drop from the simulation in scaled coordinates \bar{r} and \bar{z} . For example, the scaled radius of the larger drop in the bottom frame of Fig. 3(d) appears a bit smaller than 1, and the maximum for that simulation is indeed 0.84. As the scaled coordinates depend on time, drops do not conserve volume in the scaled coordinates, instead starting at a maximum

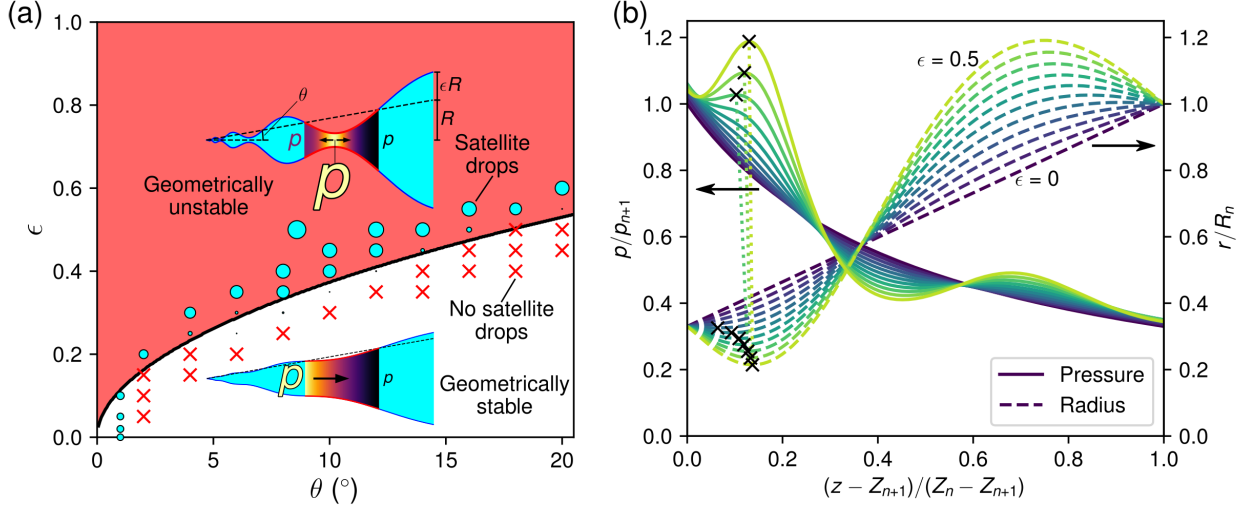


Figure 4: (a) Phase diagram showing the critical perturbation amplitude for a liquid cone to break up into drops as a function of cone angle. Red crosses and cyan circles respectively correspond to simulations with and without breakup. The radius of the circle corresponds to the equivalent radius of the largest drop from the simulation in scaled coordinates \bar{r} and \bar{z} . The black curve is the geometric stability threshold $\epsilon_g(\theta)$, above which the initial geometry of the perturbed cone exhibits a local maximum in pressure, as illustrated schematically. (b) Pressure and interface profiles for a single wave from the initial geometry of the perturbed cone described by Eq. (1) with $\theta = 10^\circ$ and ϵ between 0 and 0.5, with $\Delta\epsilon = 0.05$ between curves. Pressure profiles are normalized by $p_{n+1} \equiv \gamma \cos \theta / (Z_{n+1} \tan \theta)$, the pressure at Z_{n+1} for an unperturbed cone. Black crosses denote local maxima in pressure and minima in radius, highlighting the transition from a stable monotonically decreasing pressure profile for $\epsilon \leq 0.35$ to an unstable profile with a local maximum for $\epsilon = 0.4, 0.45$, and 0.5 .

value at pinch-off and decreasing with time. However, a perfect discrete self-similarity would result in the same scaled drop volume (or radius) for each iteration of breakup, motivating our usage of scaled radius. The very small circles in the phase diagram for $\theta \geq 6^\circ$ are tiny drops that rapidly coalesce back into the filament.

One striking result to notice from Fig. 4(a) is that relatively large perturbations are needed for a retracting cone to break up into drops. For $\theta = 2^\circ$, $\epsilon \geq 0.2$ is required to break up the cone, and the critical perturbation amplitude increases to 0.55 for $\theta = 20^\circ$. That is, perturbations that are 20% of the local cone radius are needed for a retracting cone with a cone angle of just 2° to break up into multiple drops. The one exception is for the smallest cone angle tested, $\theta = 1^\circ$. Here, all perturbation amplitudes tested, including a case with no perturbation added, led to breakup. Evidently, for small enough angles, it is possible for a retracting liquid cone to never enter the self-similar profile associated with its angle [22, 23], suggesting that the self-similar solution is unstable here. We also remark that profiles from the simulations with $\theta = 1^\circ$ and 2° do not appear discretely self-similar; only for $\theta \geq 4^\circ$ do the profiles collapse as in Fig. 3.

To determine whether aspects of the perturbation amplitude threshold for breakup can be understood more fundamentally, we examine the static stability of the initial geometry. One way to understand the Plateau-Rayleigh instability is to observe that a perturbed cylinder of liquid will be unstable when the Laplace pressure at the thinner sections is higher than the pressure at the thicker sections, since fluid will flow out of the thinner regions and amplify the initial perturbation. We adapt this argument to the perturbation on the cone and find the smallest ϵ for which the pressure profile obtains a local maximum corresponding to a local minimum in interface radius. The unperturbed cone has a pressure profile of $p(z) = (\gamma \cos \theta) / (z \tan \theta)$, so the perturbation will have to overcome the $1/z$ dependence to form a local maximum. This constraint can be contrasted with a cylinder, which is linearly unstable for $\lambda \geq 2\pi R$. The

schematics in Fig. 4(a) illustrate examples of pressure profiles for large and small perturbations to a cone with $\theta = 10^\circ$. For $\epsilon = 0.15$, the perturbation is not large enough to make a local maximum in the pressure distribution, whereas for $\epsilon = 0.7$, the high curvature from the narrow minimum in $r(z)$ leads to an unstable pressure maximum.

To make this argument quantitative, we can write the mean curvature of an axisymmetric function $r = f(z)$ as $2\kappa = 1/(f\sqrt{1+f'^2}) - f''/(1+f'^2)^{3/2}$, where $f'(z) \equiv df/dz$ and $f''(z) \equiv d^2f/dz^2$, and the Laplace pressure is given by $p = 2\kappa\gamma$. Therefore, we can solve for the critical amplitude ϵ_g as a function of θ by finding the ϵ at which $p(z)$ first exhibits a local maximum corresponding to a minimum in $r(z)$, given again by Eqs. (1)–(2). Figure 4(b) shows one cycle of the initial radius $r(z)$ and the corresponding pressure profiles $p(z)$ for varying perturbation amplitudes ϵ at an angle of $\theta = 10^\circ$. Each ‘x’ marks a local maximum in pressure or minimum in radius, and dotted lines connect them when both are present; the geometric threshold for stability then lies just below the smallest ϵ with both a local maximum in pressure and a local minimum in radius, or between $\epsilon = 0.35$ and 0.4 for $\theta = 10^\circ$. Note that the presence of a local minimum in $r(z)$ does not imply that $p(z)$ has a local maximum. Repeating this process for other cone angles and a finer spacing in ϵ , we obtain the solid black curve in Fig. 4(a). The critical perturbation amplitude ϵ_g for breakup predicted by this geometric argument increases monotonically with θ and provides a good approximation for the threshold found from numerical simulations. Only for cone angles of 1° do we see a significant difference between the two thresholds, where the full simulations were unstable for all perturbation amplitudes tested.

An important observation to make is that even in the simulations leading to breakup, drops that pinch off early typically coalesce with larger drops later, preventing a true cascade of drops from forming (see Fig. 3, for example). This coalescence is also observed experimentally, although the smaller drop can also bounce off the larger drop (see movie 1 in [16]), in which case asymmetries can launch the small drop out of the path of the rest of the jet.

It is also interesting to note that in studies of retracting cylindrical filaments, for the low-Ohnesorge number regime, the threshold filament aspect ratio appears to be set not by the Plateau-Rayleigh instability, but rather by end-pinching [43, 44], which does not depend on any initial perturbation [17, 18, 20]. Only for more viscous filaments is the Plateau-Rayleigh instability the dominant mechanism, with linear theory offering a good approximation for the time required for breakup [19]. For the perturbed cones considered here, the dependence of the capillary time τ on radius implies that the next pinch-off will always occur at the outermost connected neck. The nature of the breakup in many cases still appears qualitatively similar to that in the Plateau-Rayleigh instability, however. End-pinching does occur in the $\theta = 1^\circ$ cases, preventing the profiles from entering a discretely self-similar form and leading to breakup for all ϵ .

Figure 5 compares scaled profiles for cone angles of 1° and 2° with $\epsilon = 0$. Ref. [23] presented an asymptotic solution for the self-similar retraction of a cone at small angles, and we compute solutions to their one-dimensional model of that asymptotic solution by numerically integrating Eqs. (7.1) and (7.2) from their paper. These solutions are included in Fig. 5, indicating that the $\theta = 1^\circ$ simulation is not self-similar, whereas the $\theta = 2^\circ$ simulation approaches a self-similar profile that differs significantly from the asymptotic solution. Interestingly, the agreement for $\theta = 2^\circ$ does not improve by reducing the Ohnesorge number to $\text{Oh} = 10^{-5}$; this can be contrasted with the $\theta = 0.15$ ($\approx 8.59^\circ$) case, which is shown to agree more closely with Ref. [22] for $\text{Oh} = 10^{-5}$ in Fig. 6 in Appendix B.

Our framework can be extended to consider the effects of varying the dimensionless wavelength λ^* . Based on the linear stability of a cylinder, one might expect that choosing a λ^* closer to the fastest growing wavelength of 9.01 would reduce the threshold for breakup. Modifying the wavelength in the geometric stability calculation accordingly predicts a lower threshold for cone angles $\theta \lesssim 12^\circ$, but a greater threshold for larger angles. Working with dimensionless wavelengths appreciably shorter than 2π should lead to quite different threshold curves, as the $\theta = 0$ limit is no longer linearly unstable. For $\lambda^* = 3\pi/2$ and π , the geometric stability calculation suggests the threshold perturbation amplitude to be $0.4 \lesssim \epsilon \lesssim 0.6$ for angles $0^\circ \leq \theta \leq 20^\circ$. Simulations with dimensionless wavelengths ranging from $\pi/2$ to 4π and $\epsilon = 0.5$ all still exhibited a discrete self-similarity and led to breakup, though the simulations with $\lambda^* \leq \pi$ appeared closer to the threshold, as expected.

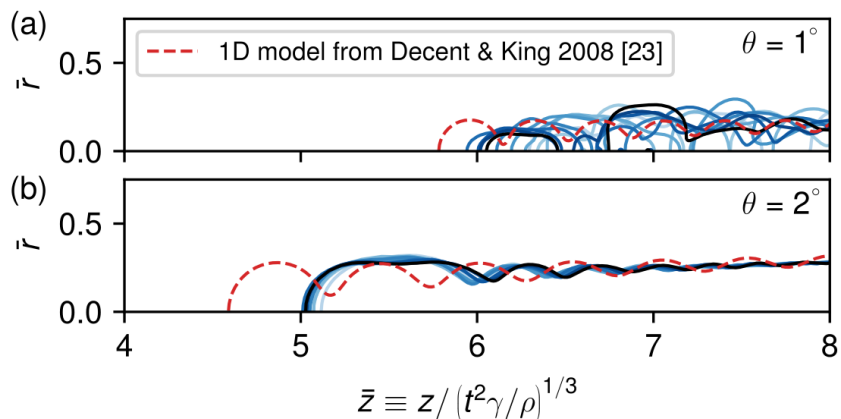


Figure 5: Scaled profiles of unperturbed cones ($\epsilon = 0$) with angles (a) $\theta = 0^\circ$ and (b) 1° . (a) Ten times log-spaced between 0.195τ and 0.962τ are plotted, with earlier times corresponding to lighter colors. The self-similar solution for an inviscid cone, calculated using the one-dimensional model from Ref. [23], is shown for comparison. Our simulation is clearly not self-similar for $\theta = 1^\circ$, instead breaking up into drops. (b) For $\theta = 2^\circ$, the ten times are log-spaced between 0.0498τ and 0.962τ . The simulation appears to be converging to a self-similar solution, though it differs notably from the solution from Ref. [23], with a stretched first lobe at the tip.

5 Conclusions

To gain insight into satellite and subsatellite drop formation following pinch-off of a primary drop from a liquid thread, we have numerically investigated the dynamics and breakup of retracting conical filaments with self-similar perturbations. For all but the smallest angles, the self-similar nature of the initial perturbation drives a retraction that is discretely self-similar; specifically, the scaled profiles are only self-similar with profiles at integer powers of the temporal scaling ratio r_t . Cones with angles $\theta \gtrsim 2^\circ$ only pinch off for relatively large perturbation amplitudes of $\epsilon \geq 0.2$, and an argument based on static stability of the initial shape predicts the threshold perturbation amplitudes well. To be clear, we are not suggesting that the precise self-similar perturbations used in this paper would be expected to occur in nature, especially at these amplitudes. Rather, we suggest that these perturbations provide an instructive way to probe the stability of a self-similar profile to finite-amplitude perturbations at all scales. The solution of these perturbed cones can also serve as a model for images like those of Fig. 1(b), in which a filament that pinches off at one end before the other can result in subsatellite drops on the side of the second pinch-off due to capillary waves from the first pinch-off that significantly perturb the interface. We can be confident that small subsatellite drops will not be produced by retracting liquid cones following pinch-off unless a strong external perturbation is present, a result that could help illuminate the mechanisms responsible for the formation of the smallest sea spray aerosols.

6 Acknowledgements

We acknowledge helpful discussions with John Lister and Peter Walls and support from the National Science Foundation under Grant No. 1351466. A.B. was supported by the ENS Paris-Saclay Internship program.

References

- [1] H. Wijshoff. The dynamics of the piezo inkjet printhead operation. *Phys. Rep.*, 491(4):77–177, 2010.

-
- [2] M. Singh, H. M. Haverinen, P. Dhagat, and G. E. Jabbour. Inkjet printing – process and its applications. *Adv. Mater.*, 22(6):673–685, 2010.
- [3] O. A. Basaran, H. Gao, and P. P. Bhat. Nonstandard inkjets. *Annu. Rev. Fluid Mech.*, 45:85–113, 2013.
- [4] S. Som and S. Aggarwal. Effects of primary breakup modeling on spray and combustion characteristics of compression ignition engines. *Combust. Flame*, 157(6):1179–1193, 2010.
- [5] E. R. Lewis and S. E. Schwartz. *Sea salt aerosol production: mechanisms, methods, measurements, and models-A critical review*. American Geophysical Union, 2004.
- [6] G. De Leeuw, E. L. Andreas, M. D. Anguelova, C. Fairall, E. R. Lewis, C. O’Dowd, M. Schulz, and S. E. Schwartz. Production flux of sea spray aerosol. *Rev. Geophys.*, 49(2), 2011.
- [7] A. Woodcock, C. Kientzler, A. Arons, and D. Blanchard. Giant condensation nuclei from bursting bubbles. *Nature*, 172(4390):1144–1145, 1953.
- [8] D. K. Woolf, P. A. Bowyer, and E. C. Monahan. Discriminating between the film drops and jet drops produced by a simulated whitecap. *J. Geophys. Res. Oceans*, 92(C5):5142–5150, 1987.
- [9] X. Wang, G. B. Deane, K. A. Moore, O. S. Ryder, M. D. Stokes, C. M. Beall, D. B. Collins, M. V. Santander, S. M. Burrows, C. M. Sultana, et al. The role of jet and film drops in controlling the mixing state of submicron sea spray aerosol particles. *Proc. Natl. Acad. Sci. U.S.A.*, page 201702420, 2017.
- [10] E. Ghabache and T. Séon. Size of the top jet drop produced by bubble bursting. *Phys. Rev. Fluids*, 1(5):051901, 2016.
- [11] C. F. Brasz, C. T. Bartlett, P. L. Walls, E. G. Flynn, Y. E. Yu, and J. C. Bird. Minimum size for the top jet drop from a bursting bubble. *Phys. Rev. Fluids*, 3(7):074001, 2018.
- [12] C. Kientzler, A. B. Arons, D. C. Blanchard, and A. H. Woodcock. Photographic investigation of the projection of droplets by bubbles bursting at a water surface. *Tellus*, 6(1):1–7, 1954.
- [13] D. E. Spiel. The number and size of jet drops produced by air bubbles bursting on a fresh water surface. *J. Geophys. Res. Oceans*, 99(C5):10289–10296, 1994.
- [14] J. Eggers. Nonlinear dynamics and breakup of free-surface flows. *Rev. Mod. Phys.*, 69(3):865–929, 1997.
- [15] J. Eggers and E. Villermaux. Physics of liquid jets. *Rep. Prog. Phys.*, 71(3):036601, 2008.
- [16] See supplemental material at [url] for movies of the breakup of a filament from a column of water and the simulated retraction of a perturbed liquid cone in scaled and unscaled coordinates.
- [17] P. K. Notz and O. A. Basaran. Dynamics and breakup of a contracting liquid filament. *J. Fluid Mech.*, 512:223–256, 2004.
- [18] A. A. Castrejón-Pita, J. Castrejón-Pita, and I. Hutchings. Breakup of liquid filaments. *Phys. Rev. Lett.*, 108(7):074506, 2012.
- [19] T. Driessen, R. Jeurissen, H. Wijshoff, F. Toschi, and D. Lohse. Stability of viscous long liquid filaments. *Phys. Fluids*, 25(6):062109, 2013.
- [20] J. Hoepffner and G. Paré. Recoil of a liquid filament: escape from pinch-off through creation of a vortex ring. *J. Fluid Mech.*, 734:183, 2013.
- [21] R. F. Day, E. J. Hinch, and J. R. Lister. Self-similar capillary pinchoff of an inviscid fluid. *Phys. Rev. Lett.*, 80(4):704, 1998.

-
- [22] A. Sierou and J. R. Lister. Self-similar recoil of inviscid drops. *Phys. Fluids*, 16(5):1379–1394, 2004.
- [23] S. Decent and A. King. Surface-tension-driven flow in a slender cone. *IMA J. Appl. Math.*, 73(1):37–68, 2008.
- [24] C. T. Bartlett, G. A. Généro, and J. C. Bird. Coalescence and break-up of nearly inviscid conical droplets. *J. Fluid Mech.*, 763:369–385, 2015.
- [25] D. Peregrine, G. Shoker, and A. Symon. The bifurcation of liquid bridges. *J. Fluid Mech.*, 212:25–39, 1990.
- [26] M. P. Brenner, J. Eggers, K. Joseph, S. R. Nagel, and X. Shi. Breakdown of scaling in droplet fission at high reynolds number. *Phys. Fluids*, 9(6):1573–1590, 1997.
- [27] P. K. Notz, A. U. Chen, and O. A. Basaran. Satellite drops: Unexpected dynamics and change of scaling during pinch-off. *Phys. Fluids*, 13(3):549–552, 2001.
- [28] J. Eggers and T. F. Dupont. Drop formation in a one-dimensional approximation of the Navier–Stokes equation. *J. Fluid Mech.*, 262:205–221, 1994.
- [29] T. Driessen and R. Jeurissen. A regularised one-dimensional drop formation and coalescence model using a total variation diminishing (tvd) scheme on a single eulerian grid. *Int. J. Comput. Fluid Dyn.*, 25(6):333–343, 2011.
- [30] A. Sierou and J. R. Lister. Self-similar solutions for viscous capillary pinch-off. *J. Fluid Mech.*, 497:381–403, 2003.
- [31] S. Popinet. Gerris: a tree-based adaptive solver for the incompressible Euler equations in complex geometries. *J. Comput. Phys.*, 190(2):572 – 600, 2003.
- [32] S. Popinet. *The Gerris Flow Solver*, 2007. <http://gfs.sf.net>.
- [33] S. Popinet. An accurate adaptive solver for surface-tension-driven interfacial flows. *J. Comput. Phys.*, 228(16):5838 – 5866, 2009.
- [34] G. Barenblatt and Y. B. Zel’Dovich. Self-similar solutions as intermediate asymptotics. *Annu. Rev. Fluid Mech.*, 4(1):285–312, 1972.
- [35] D. Sornette. Discrete-scale invariance and complex dimensions. *Phys. Rep.*, 297(5):239–270, 1998.
- [36] M. W. Choptuik. Universality and scaling in gravitational collapse of a massless scalar field. *Phys. Rev. Lett.*, 70(1):9, 1993.
- [37] M. Tjahjadi, H. Stone, and J. Ottino. Satellite and subsatellite formation in capillary breakup. *J. Fluid Mech.*, 243:297–297, 1992.
- [38] X. Shi, M. P. Brenner, and S. R. Nagel. A cascade of structure in a drop falling from a faucet. *Science*, 265(5169):219–222, 1994.
- [39] M. P. Brenner, X. Shi, and S. R. Nagel. Iterated instabilities during droplet fission. *Phys. Rev. Lett.*, 73(25):3391, 1994.
- [40] J. Eggers. Coalescence of spheres by surface diffusion. *Phys. Rev. Lett.*, 80(12):2634, 1998.
- [41] M. S. Oliveira and G. H. McKinley. Iterated stretching and multiple beads-on-a-string phenomena in dilute solutions of highly extensible flexible polymers. *Phys. Fluids*, 17(7):071704, 2005.
- [42] M. C. Dallaston, M. A. Fontelos, D. Tseluiko, and S. Kalliadasis. Discrete self-similarity in interfacial hydrodynamics and the formation of iterated structures. *Phys. Rev. Lett.*, 120(3):034505, 2018.

- [43] H. A. Stone, B. Bentley, and L. Leal. An experimental study of transient effects in the breakup of viscous drops. *J. Fluid Mech.*, 173:131–158, 1986.
- [44] H. A. Stone and L. Leal. Relaxation and breakup of an initially extended drop in an otherwise quiescent fluid. *J. Fluid Mech.*, 198:399–427, 1989.

A Numerical simulation details

The phase offset ϕ_0 is chosen to make the interface slope $dr/dz = 0$ at $z = Z$ for smoothness, as symmetry is used about that plane. For small enough ϵ , $r(z)$ monotonically increases and this condition cannot be satisfied, in which case ϕ_0 is chosen to minimize the slope dr/dz at $z = Z$. Of the simulations run to construct the phase diagram in Fig. 4(a), only $\epsilon = 0$ for $\theta = 1^\circ$ and $\epsilon = 0.02$ for $\theta = 2^\circ$ are too small to find a ϕ_0 resulting in $dr/dz = 0$ at $z = Z$.

The computational domain is a cylinder of radius 3 and height 9, discretized as a 2D rectangle (three square “boxes” of side length 3) by using axisymmetry. Free-slip, impermeable (symmetry) boundary conditions are used on all boundaries. For $\theta \geq 0.15 \approx 8.59^\circ$, the initial cone is constrained radially such that $R = 1$. This choice leads to cone lengths $Z = 1/\tan\theta \leq 6.617$. For $\theta < 0.15$, the domain is constrained in the axial direction, with $Z = 7$ enforced, resulting in $R = 7 \tan\theta < 1.058$.

The grid employs an adaptive quadtree mesh, where each box of length 3 can be subdivided up to $r_{\max} = 14$ times, resulting in a cell size $\Delta = 3/2^{14} = 1.83 \times 10^{-4}$. During the simulation, the interface is resolved to a refinement level of r_{\max} for $z \leq 0.02Z_0$, $r_{\max} - 1$ for $z \leq 0.04Z_0$, and $r_{\max} - 2$ for the rest of the domain.

The number of waves n_w of the perturbation to include in the initial geometry is set such that the spherical cap at the end of the last wave has a radius around $n_c\Delta$ with $n_c = 8$ cells. Defining $R_c = R(1 + \epsilon \sin(\phi_0 + \log(Z)/\tan\theta))$ as the perturbed radius at $z = Z$, the spherical cap is added at $z = Zr_l^{n_w}$ with radius $R_cr_l^{n_w}$. The number of waves can therefore be calculated as

$$n_w = \text{round} \left(\frac{\log(n_c\Delta/R_c)}{\log r_l} \right), \quad (3)$$

as this results in $R_cr_l^{n_w} \approx n_c\Delta$. For simulations with $(\theta, \epsilon) = (1^\circ, 0.1)$, $(8^\circ, 0.4)$, and $(20^\circ, 0.6)$, we obtain $n_w = 41$, 8, and 3, respectively. Large cone angles lead to small numbers of waves n_w due to the spatial rescaling ratio $r_l \equiv \exp(-\lambda^* \tan\theta)$ approaching small values.

Simulations are run out to $t/\tau = 1$ (or 1.15 for $\theta = 0.15$ to include the last green profile), which allows for $n_t \equiv \bar{t}/T = \log(\tau/t_0)/\log(1/r_t)$ cycles between time t_0 and time τ . Empirically, we observe that profiles typically fall into their self-similar form within $t/\tau \approx 0.001$ for $\theta > 2^\circ$, and for $t_0/\tau = 0.001$, we get $n_t = 6$ and 3 for $\theta = 8^\circ$ and 20° , respectively. Cones with smaller angles take longer to approach their self-similar form (or roughly steady state shape in scaled coordinates, even if not self-similar): $t/\tau \approx 0.02$ and 0.05 for $\theta = 2^\circ$ and 1° , respectively.

B Validation and grid independence

Scaled profiles for $\theta = 0.15$ and $\epsilon = 0$ are compared with the inviscid self-similar solution from Ref. [22] in Fig. 6. Excellent agreement is shown for $\text{Oh} = 10^{-5}$, while the profiles deviate more as Oh increases, as expected.

Grid independence of the evolution for $\theta = 0.15$ and $\epsilon = 0.5$ is checked by comparing to a simulation with one level finer refinement everywhere. Profiles for selected times are shown in Fig. 7, demonstrating close agreement between simulations after the first wave. The offset between profiles reveals that earlier iterations of the breakup around $\bar{z} = 5$ are slightly delayed relative to their expected discrete self-similarity timing ($\bar{t} = T/3 \pmod{T}$), as the earlier red curves in the middle frame are further from pinching off than the later curves. This observation is consistent with the larger role that viscosity plays at smaller length

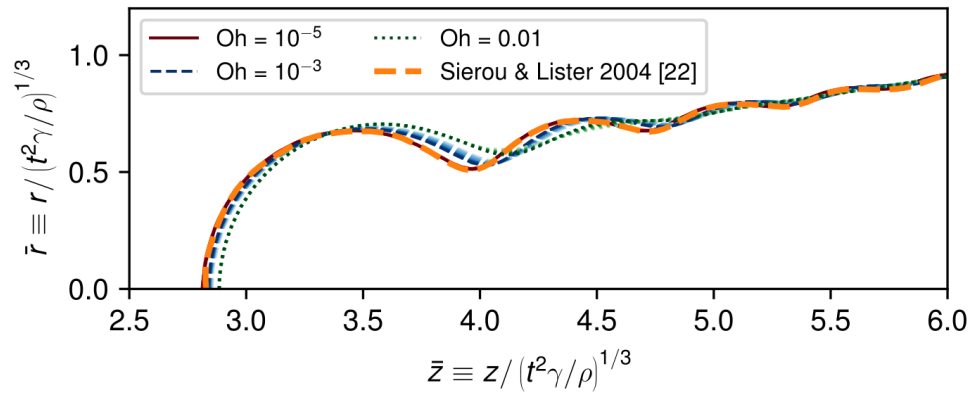


Figure 6: Comparison between the inviscid self-similar solution for a retracting cone [22] and scaled profile snapshots from simulations with the same angle ($\theta = 0.15$), $\epsilon = 0$, and various Ohnesorge numbers. Eight times log-spaced between 0.0179τ and 0.497τ are plotted from each simulation with earlier times corresponding to lighter colors, as in Fig. 3. (Note that Figs. 3(a)–(b) used the same eight times along with six earlier ones, with the earliest being 0.00104τ .)

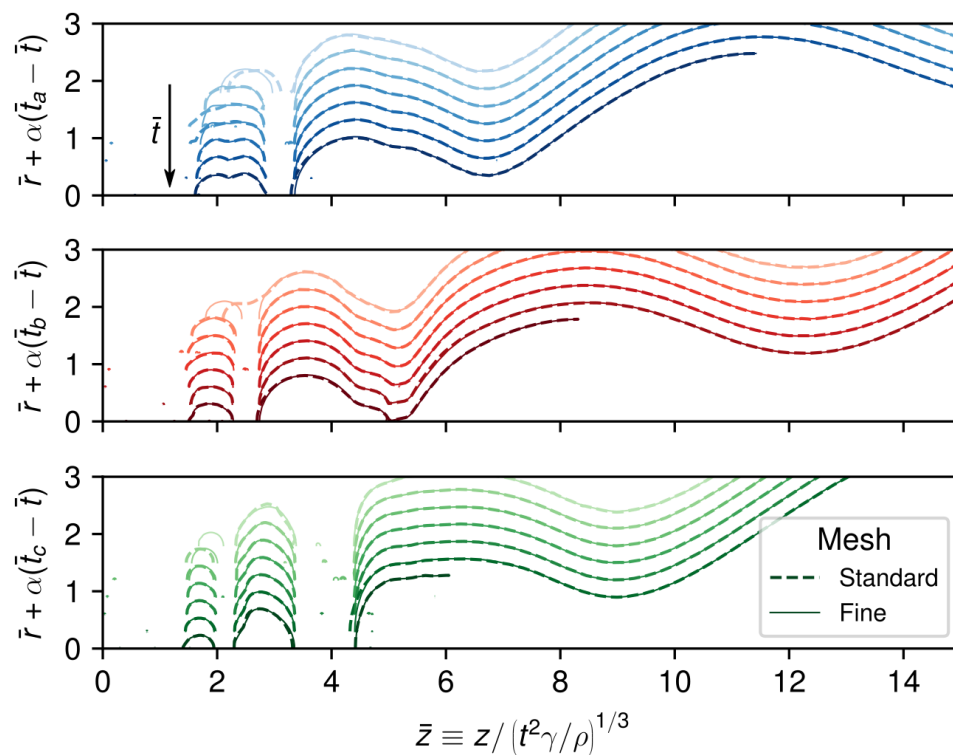


Figure 7: Comparison of profile snapshots for $\theta = 0.15$, $\epsilon = 0.5$ between simulations with the standard mesh refinement and with a finer mesh refinement, plotted with the self-similar scaling. The times plotted correspond to those from Fig. 3(d) along with two earlier times for each frame, making the earliest time in the top frame $t_0 r_t^2 = 8.57 \times 10^{-5} \tau$ or $\bar{t} \equiv \log t/t_0 = -2T$ (note that $r_t = 0.241$ for $\theta = 0.15$). A vertical offset proportional to the logarithmic time \bar{t} has been applied such that the earliest times are highest in order to allow direct comparison between refinement levels. The constants used to specify the offsets are $\alpha = 0.3/T$, $\bar{t}_a = 4T$, $\bar{t}_b = \bar{t}_a + T/3$, and $\bar{t}_c = \bar{t}_a + 2T/3$.